

Precision Timing of PSR J0437–4715 with the IAR Observatory and Implications for Low-frequency Gravitational Wave Source Sensitivity

M. T. Lam^{1,2} and J. S. Hazboun³

School of Physics and Astronomy, Rochester Institute of Technology, Rochester, NY 14623, USA; mlam@mail.rit.edu
 Laboratory for Multiwavelength Astrophysics, Rochester Institute of Technology, Rochester, NY 14623, USA
 Physical Sciences Division, University of Washington Bothell, 18115 Campus Way NE, Bothell, WA 98011, USA
 Received 2020 July 1; revised 2021 February 18; accepted 2021 March 1; published 2021 April 27

Abstract

While observations of many high-precision radio pulsars of order $\lesssim 1 \,\mu s$ across the sky are needed for the detection and characterization of a stochastic background of low-frequency gravitational waves (GWs), sensitivity to single sources of GWs requires even higher timing precision. The Argentine Institute of Radio Astronomy (IAR; Instituto Argentino de Radioastronomía) has begun observations of the brightest known millisecond pulsar, J0437-4715. Even though the two antennas are smaller than other single-dish telescopes previously used for pulsar timing array (PTA) science, the IAR's capability to monitor this pulsar daily, coupled with the pulsar's brightness, allows for high-precision measurements of pulse-arrival time. While upgrades of the facility are currently underway, we show that modest improvements beyond current plans will provide IAR with unparalleled sensitivity to this pulsar. The most stringent upper limits on single GW sources come from the North American Nanohertz Observatory for Gravitational Waves (NANOGrav). Observations of PSR J0437-4715 will provide a significant sensitivity increase in NANOGrav's "blind spot" in the sky where fewer pulsars are currently being observed. With state-ofthe art instrumentation installed, we estimate the array's sensitivity will improve by a factor of \approx 2–4 over 10 yr for 20% of the sky with the inclusion of this pulsar, as compared to a static version of the PTA used in NANOGrav's most recent limits. More modest instrumentation results in factors of $\approx 1.4-3$. We identify four other candidate pulsars as suitable for inclusion in PTA efforts. International PTA efforts will also benefit from inclusion of these data, given the potential achievable sensitivity.

Unified Astronomy Thesaurus concepts: Millisecond pulsars (1062); Pulsar timing method (1305); Pulsars (1306); Gravitational waves (678); Gravitational wave astronomy (675); Gravitational wave sources (677)

1. Introduction

The search for gravitational waves (GWs) using an array of recycled millisecond pulsars (MSPs) is a key science goal for the largest radio telescopes in the world. Pulsars act as high-precision clocks, and the passage of a GW along the line of sight is expected to cause slight variations in the arrival times of their observed emission that can be measured using high-precision pulsar timing (Sazhin 1978; Detweiler 1979; Foster & Backer 1990). Large telescopes are needed to measure high signal-to-noise ratio (S/N) pulses and estimate their arrival times to high precision (Ransom et al. 2019). While current pulsar-timing efforts are dominated by large single-dish (60–300 m class) telescopes, the use of larger, more sensitive telescopes and interferometers is becoming an increasingly important contribution to pulsar timing array (PTA) science (Perera et al. 2019).

The expected first detection of low-frequency (\sim nHz– μ Hz) GWs is from a stochastic background of unresolved supermassive black hole binaries (e.g., Rosado et al. 2015). Detection and characterization of this background require observations of many pulsars in order to build pairwise quadrupolar correlations in the observed arrival-time perturbations. The best-timed MSPs are used in these searches, with timing precision $\lesssim 1~\mu s$. Individual sources of GWs, such as from a single resolved supermassive black hole binary inspiral or merger, require MSPs with precision of an order of magnitude or more, such that specific waveforms can be recovered (e.g., Burt et al. 2011). Red noise in the pulsar times of arrival (TOAs), e.g., such as from intrinsic spin noise or the

GW background, will impact the waveform recovery—but mostly at the lowest GW frequencies ($\lesssim 10\,\text{nHz}$; Xin et al. 2020). Later in this paper, we shall discuss the issue further with respect to our analysis. Observing many well-timed pulsars both increases the signal-to-noise ratio of a GW detection and future characterization, and improves upon the coverage of events across the sky.

1.1. The North American Nanohertz Observatory for Gravitational Waves

The North American Nanohertz Observatory for Gravitational Waves (NANOGrav; McLaughlin 2013; Ransom et al. 2019) collaboration is working toward the detection and characterization of low-frequency GWs by means of monitoring an array of nearly 80 precisely timed MSPs using three telescopes: the 305 m William E. Gordon Telescope of the Arecibo Observatory (Arecibo), the 100 m Robert C. Byrd Green Bank Telescope of the Green Bank Observatory (GBO), and the 27 element 25 m antennas of the National Radio Astronomy Observatory's (NRAO) Karl G. Jansky Very Large Array (VLA). NANOGrav has already placed upper limits on the amount of GWs in the universe, which have provided strong astrophysical constraints on merging galaxies and cosmological models (Arzoumanian et al. 2018a, 2020; Aggarwal et al. 2019, 2020). NANOGrav is poised to detect and begin characterization of the stochastic GW background from an ensemble of unresolved supermassive black hole binaries (SMBHBs) within the next 3–5 yr (Rosado et al. 2015; Taylor et al. 2016; Arzoumanian et al. 2018a; Arzoumanian et al. 2021,

 Table 1

 Current Observing Parameters for the IAR Antennas

Parameter	A1	A2
Maximum Tracking Time (T_{obs})	3 ^h 40 ^m	3 ^h 40 ^m
Circular Polarizations (N_{pol})	1	2
Receiver Temperature (T_{revr})	100 K	110 K
Gain (G)	11.9 Jy K^{-1}	13.0 Jy K^{-1}
Frequency Range (MHz)	1100-1510	1200-1600
Bandwidth (B)	112 MHz	56 MHz

Note. All values taken from Gancio et al. (2020). PSR J0437-4715 can be observed for the maximum tracking time.

in preparation). The first detection of a continuous-wave (CW) source of GWs from a single SMBHB is expected by the late 2020s (Rosado et al. 2015; Mingarelli et al. 2017; Kelley et al. 2018; Aggarwal et al. 2019). In addition, NANOGrav is sensitive to the direct signature of SMBHB mergers, known as a "burst with memory" (BWM; Aggarwal et al. 2020).

1.2. The Argentine Institute for Radio Astronomy

The Argentine Institute of Radio Astronomy (IAR; Instituto Argentino de Radioastronomía) has begun upgrades of two 30 m antennas primarily for the purpose of pulsar observations (Gancio et al. 2020). Located at latitude $\approx -37^{\circ}$, the observatory covers declinations $\delta < -10^{\circ}$. The two antennas, A1 and A2, are 30 m equatorial mount telescopes separated by 120 m. Both are capable of observations around 1.4 GHz, each with current specifications listed in Table 1.

While 30 m antennas fall below the typical size of radio telescopes used in precision timing experiments (e.g., Perera et al. 2019), the IAR Observatory has several advantages for high-precision timing, specifically in the area of GW detection and characterization. With access to the southern sky below $\delta < -10^{\circ}$ as well as many galactic disk pulsars, in addition to the ability to track objects for nearly four hours, IAR has demonstrated the capability of high-cadence timing on a number of those pulsars, particularly of the bright millisecond pulsar J0437–4715 (Gancio et al. 2020; Sosa Fiscella et al. 2021). Their preliminary observations suggest that future measurements will be a significant contributor to PTA sensitivity.

1.3. The Millisecond Pulsar J0437-4715

Discovered in the Parkes Southern Pulsar Survey (Johnston et al. 1993), PSR J0437–4715 is the brightest known MSP and has the lowest dispersion measure (DM; the integrated line-of-sight electron density) of any MSP; it is the second-lowest of any pulsar (Manchester et al. 2005). Its bright pulses can be precisely timed with high S/N, allowing for this pulsar to be used in tests of general relativity (van Straten et al. 2001; Verbiest et al. 2008) and pulsar emission physics (Osłowski et al. 2014), as a source in the development of new high-precision timing calibration and methodology (van Straten 2006; Liu et al. 2011; Osłowski et al. 2013), and as a sensitive component to pulsar timing arrays (Perera et al. 2019; Kerr et al. 2020). Some pulsar properties are listed in Table 2.

In addition to the ability to measure high S/N pulses, given its low DM, we expect that unmodeled chromatic (i.e., radio-frequency-dependent) interstellar propagation effects are

Table 2 Parameters for PSR J0437-4715

Parameter	Value
Spin Period ^a (P)	5.76 ms
Dispersion Measure ^a (DM)	$2.64 \mathrm{pc} \; \mathrm{cm}^{-3}$
Effective Width (W_{eff})	667.6 μs
Flux Density at 400 MHz ^a $(S_{400},)$	550.0 mJy
Flux Density at 1000 MHz ^c (S ₄₀₀)	223 mJy
Flux Density at 1400 MHz ^a (S_{1400})	160.0 mJy
Spectral Index c (α)	-0.99
Jitter rms for 1 hr at 730 MHz ($\sigma_{J,730}$)	$61 \pm 9 \text{ ns}$
Jitter rms for 1 hr at 1400 MHz ($\sigma_{J,1400}$)	$48.0 \pm 0.6 \text{ ns}$
Jitter rms for 1 hr at 3100 MHz ($\sigma_{J,3100}$)	$41 \pm 2 \text{ ns}$
Phase Bins (N_{ϕ} , assumed)	512
Median $\sigma_{S/N}$ for Antenna 1 ($\sigma_{S/N, A1}$)	200 ns
Median $\sigma_{S/N}$ for Antenna 2 ($\sigma_{S/N, A2}$)	330 ns
Median S/N for Antenna 1° (\tilde{S}_{A1})	148.8
Median S/N for Antenna 2^c (\tilde{S}_{A2})	90.5

Notes.

- ^a Values taken from PSRCAT (Manchester et al. 2005).
- ^b Effective width estimated from profile in Kerr et al. (2020).

reduced for this pulsar (Cordes & Shannon 2010), thereby limiting one of the significant sources of timing noise found in many other pulsars. PSR J0437—4715, however, is not timed without complications. The pulsar has measurable achromatic noise consistent with rotational spin fluctuations (Shannon & Cordes 2010; Lam et al. 2017), quasi-periodic intensity and polarization variations are seen in subpulse components (De et al. 2016), and a systematic variation in the pulse shape has also been observed (Kerr et al. 2020). While these effects complicate the pulsar's use in tests of fundamental physics with high-precision timing, its demonstrated stability nonetheless suggests that it can be used in these tests (e.g., Verbiest et al. 2009), including in searches for stochastic and deterministic GW signals.

In this paper, we demonstrate the specific capabilities of the IAR to observe PSR J0437-4715 and provide unparalleled sensitivity to the pulsar for the purpose of single-source CW detection and future characterization. In Section 2, we provide the framework for our TOA sensitivity estimates. We consider the current IAR observations of PSR J0437-4715 in Section 3. and then extrapolate to future possible operating modes in Section 4, comparing the modes to observations of the pulsar by other international observatories as well. In Section 5, we demonstrate how the IAR will improve sensitivity to singlesource CWs when the data are combined with that of NANOGrav. As the collaboration observing the most pulsars (Ransom et al. 2019) and with the most recent and stringent CW limits (Aggarwal et al. 2019; Arzoumanian et al. 2020), we will focus our analyses primarily on improving upon a projected NANOGrav data set with observations of PSR J0437 -4715, noting that upcoming analyses (e.g., Alam et al. (2021a, 2021b), which already include more time baseline and more pulsars) imply greater sensitivity in the future. We describe other possible pulsar targets in Section 6, and conclude in Section 7.

^c Derived parameters.

2. The Sensitivity toward Continuous Waves

In this section, we describe the mathematical framework for determining the precision of an individual pulsar and then the sensitivity toward CW sources from the sum of correlated GW signals between pulsar pairs. As the components of this framework have been discussed significantly throughout the literature, we will lay out each piece but briefly, and will point the reader to other references with more detailed discussion.

2.1. Single-pulsar Timing Sensitivity

We use the framework of Lam et al. (2018) to estimate the noise contributions to pulsar TOA uncertainties—or equivalently, how precisely we can measure the TOAs. Gancio et al. (2020) show the first set of timing residuals (the observed TOAs minus a model for the expected arrival times) for PSR J0437–4715 with the IAR, and they demonstrate excess noise beyond the uncertainties derived from the common practice of matching a pulse template to the observed pulsar profile to estimate their TOAs (Taylor 1992).

2.1.1. Short-timescale Noise

Lam et al. (2016a) describe a model for white noise in timing residuals on short timescales, ≤1 hr, i.e., the time of typical observations. In that analysis, they assume perfect polarization calibration and radio frequency interference (RFI) removal; the former is currently impossible in the case of A1, with only one measured polarization channel. However, assuming both are true, the three white noise components described are the template fitting, jitter, and scintillation noise terms.

Template fitting errors rely on the matched-filtering assumption that the observed pulse profiles are an exact match to a template shape with some additive noise. These are the *minimum* possible errors for TOA estimates, and are given by

$$\sigma_{\rm S/N}(S) = \frac{W_{\rm eff}}{S\sqrt{N_{\phi}}},\tag{1}$$

where $W_{\rm eff}$ is the effective width of the pulse, N_{ϕ} is the number of samples (bins) across the profiles, and S is the signal-to-noise ratio (written this way in equations for clarity), taken to be the peak to off-pulse rms. The effective width is related to the spin period of the pulsar P and the template profile normalized to unit height, $U(\phi)$, by

$$W_{\text{eff}} = \frac{P}{N_{\phi}^{1/2} \left[\sum_{i=1}^{N_{\phi}-1} [U_{\text{obs}}(\phi_i) - U_{\text{obs}}(\phi_{i-1})]^2 \right]^{1/2}}.$$
 (2)

Pulse profiles are frequency-dependent, and so this error will apply to each profile measured at a given frequency. However, given the low bandwidths currently available at the IAR Observatory, it is sufficient, given the S/N regime of the observations, to average the data across not only time but frequency as well, to obtain a single TOA per epoch per antenna. Similarly, many other frequency-dependent variations within the band will be small and we will ignore those here.

While $W_{\rm eff}$ and N_{ϕ} are constants, the pulse S/N will vary on short timescales, due to diffractive scintillation, with a known

probability density function (PDF) written as (Cordes & Chernoff 1997; Lam et al. 2016a)

$$f_{\mathcal{S}}(S|S_0, n_{\text{ISS}}) = \frac{(Sn_{\text{ISS}}/S_0)^{n_{\text{ISS}}}}{S\Gamma(n_{\text{ISS}})} e^{-Sn_{\text{ISS}}/S_0} \Theta(S), \tag{3}$$

where S_0 is the mean S/N, Γ is the Gamma function, Θ is the Heaviside step function, and $n_{\rm ISS}$ is the number of scintles in the observation of length T and bandwidth B, given by

$$n_{\rm ISS} \approx \left(1 + \eta_t \frac{T}{\Delta t_{\rm d}}\right) \left(1 + \eta_\nu \frac{B}{\Delta \nu_{\rm d}}\right).$$
 (4)

The scintillation parameters $\Delta t_{\rm d}$ and $\Delta \nu_{\rm d}$ describe the characteristic timescale and bandwidth of intensity maxima, or scintles, in a dynamic spectrum. The η_t and η_ν parameters are the scintle filling factors ≈ 0.2 (Cordes & Shannon 2010; Levin et al. 2016).

Gwinn et al. (2006) found two diffractive scintillation scales for PSR J0437–4715 made at an observing frequency of 328 MHz. The first has $\Delta t_{\rm d}=1000\,{\rm s}$ and $\Delta\nu_{\rm d}=16$ MHz, while the second has $\Delta t_{\rm d}=90\,{\rm s}$ and $\Delta\nu_{\rm d}=0.5$ MHz. For a Kolmogorov medium, we can scale these quantities as $\Delta t_{\rm d} \propto \nu^{6/5}$ and $\Delta\nu_{\rm d} \propto \nu^{22/5}$ (Cordes & Rickett 1998; Lam et al. 2018). Therefore, when scaled to an observing frequency of 1.4 GHz, we have $\Delta t_{\rm d}=5700\,{\rm s}$ and $\Delta\nu_{\rm d}=9.5$ GHz for the first scale, and $\Delta t_{\rm d}=510\,{\rm s}$ and $\Delta\nu_{\rm d}=300$ MHz for the second scale. Keith et al. (2013) measured the scintillation parameters at 1.5 GHz for PSR J0437–4715; when scaled to 1.4 GHz, they found $\Delta t_{\rm d}=2290\,{\rm s}$ and $\Delta\nu_{\rm d}=740$ MHz, in between the two scales observed by Gwinn et al. (2006).

Using these measurements of the scintillation parameters, we will estimate $n_{\rm ISS}$ and thus the predicted impact on the PDF of S. Given the current small bandwidths of the receiver, since $B < \Delta \nu_{\rm d}$ in all cases, the second of the two components in Equation (4) will be ≈ 1 and so we have $n_{\rm ISS} \approx 1 + \eta_t T/\Delta t_{\rm d}$. For $T=13200\,\rm s$, this quantity will range between 1.5 and 5.2. The higher $n_{\rm ISS}$ is, the more that the PDF will tend toward the mean S/N value S_0 , whereas when $n_{\rm ISS}$ is close to 1, the distribution becomes exponential. Therefore, this value will heavily dictate the timing uncertainties achievable, which we will briefly discuss when applying to the real data.

The two other short-timescale contributions to the white noise discussed in Lam et al. (2016a) are the jitter and scintillation-noise terms; the latter is separate from the S/N change due to scintillation. Both cause stochastic deviations to the observed pulse shapes such that the matched-filtering assumption of template fitting no longer applies. Jitter, due to single-pulse stochasticity, becomes a significant noise contribution for well-timed, high-S/N MSPs (Lam et al. 2019). Shannon et al. (2014) measured the timing uncertainty due to jitter for an hour-long observation to be $\sigma_J = 48.0 \pm 0.6$ ns, significantly less than the template fitting errors shown in Gancio et al. (2020). In addition, since the rms jitter scales inversely with the square root of the number of pulses, this contribution to the TOA uncertainty for a 3^h 40^m observation will be even smaller in IAR data, and therefore can be ignored.

Scintillation noise is caused by the finite-scintle effect and results in pulse-shape stochasticity due to an imperfectly known *pulse broadening function* (Cordes et al. 1990; Cordes & Shannon 2010; Coles et al. 2010). Its maximum value is approximately the scattering timescale τ_d , which is inversely

proportional to $\Delta\nu_{\rm d}$ (Cordes & Rickett 1998; Cordes & Shannon 2010):

$$\tau_{\rm d} = \frac{C_{\rm l}}{2\pi\Delta\nu_{\rm d}},\tag{5}$$

where $C_1 \approx 1$ is a coefficient that depends on the geometry of the intervening medium. Since scattering tends to be more significant at higher DMs (Bhat et al. 2004), we already expect $\tau_{\rm d}$ to be small for PSR J0437–4715. For the minimum value of $\Delta \nu_{\rm d}$ above, we find a maximum value of $\tau_{\rm d} \lesssim 1$ ns, and therefore scintillation noise can also be ignored for this pulsar.

2.1.2. Dispersion Measure Estimation

Estimation of DM and the subsequent correction of dispersion are critical for proper precision timing. Since the scattering timescale is small, the dominant component to DM estimation errors is that due to the white noise described above (Lam et al. 2018). For measurements taken at two frequencies ν_1 and ν_2 , with the frequency ratio defined as $r \equiv \nu_2/\nu_1 \geqslant 1$, the timing uncertainty due to DM estimation is (see Appendix A of Lam et al. 2020)

$$\sigma_{\widehat{\text{DM}}} = \frac{\sqrt{\sigma_{\nu_1}^2 + r^4 \sigma_{\nu_2}^2}}{r^2 - 1},\tag{6}$$

where the σ_{ν} values are the timing uncertainties at each frequency. Both Cordes & Shannon (2010) and Lam et al. (2018) describe the matrix formalism for calculating this uncertainty when multichannel measurements are available. Estimating the DM with measurements taken at multiple frequencies results in reduced uncertainties even if the covered range r is the same.

If DM variations are not accounted for in a timing model, as in Gancio et al. (2020), then additional uncertainties arise. Many types of effects give rise to both stochastic and systematic variations in DM (Lam et al. 2016b). For example, an Earth–pulsar line of sight passing close to the Sun will cause an increase in the DM from the increased electron density of the solar wind (You et al. 2007; Tiburzi et al. 2019; Madison et al. 2019); while the motion through this electron density profile gives rise to systematic variations, any fluctuations in the solar wind will cause variations that are random in nature. The turbulent interstellar medium will also give rise to DM fluctuations that are random though correlated over time (Foster & Cordes 1990; Phillips & Wolszczan 1991).

The turbulent medium is typically parameterized by a powerlaw electron density wavenumber spectrum over many orders of magnitude (Armstrong et al. 1995). An equivalent formulation that one can derive from this spectrum is the DM structure function (e.g., Lam et al. 2016b), given by

$$D_{\rm DM}(\tau) \equiv \langle [{\rm DM}(t+\tau) - {\rm DM}(t)]^2 \rangle, \tag{7}$$

where τ is the time lag and the brackets denote the ensemble average. The structure function of the timing perturbations δt is related to the DM structure function by

$$D_{\delta t}(\tau) = K^2 \nu^{-4} D_{\rm DM}(\tau), \tag{8}$$

where $K \approx 4.149 \times 10^3 \,\mu$ s GHz² pc⁻¹ cm³ is the dispersion constant in observationally convenient units, i.e., for a DM of 1 pc cm⁻³ and radio emission at 1 GHz, we expect 4149 μ s of delay. This is a significantly larger delay than the achievable timing

precision, because DM *estimates* are known much more precisely and therefore the delay can be corrected for to high accuracy.

We can directly relate the rms timing fluctuations for a given time lag to the structure function by

$$\sigma_{\delta t}(\tau) = \left[\frac{1}{2}D_{\delta t}(\tau)\right]^{1/2}.\tag{9}$$

For a Kolmogorov turbulent spectrum, we can write the structure function in the power-law form (Lam et al. 2016b):

$$D_{\delta t}(\tau) = \frac{1}{(2\pi\nu)^2} \left(\frac{\tau}{\Delta t_{\rm d}}\right)^{5/3} = 0.0253 \text{ ns}^2 \nu_{\rm GHz}^{-2} \left(\frac{\tau}{\Delta} t_{\rm d}\right)^{5/3}.$$
(10)

For PSR J0437–4715, we will first consider the middle value of $\Delta t_{\rm d}$ provided by Keith et al. (2013), with $\Delta t_{\rm d} = 2290\,\rm s$. On the timescale of the $\tau \approx 100\,\rm days$ as shown in Gancio et al. (2020), the rms timing perturbations for unaccounted for DM variations would be approximately 110 ns at 1.4 GHz, and so should be a negligible part of their error budget shown. Nonetheless, if we consider this error for longer timespans, as for 1000 and 10,000 days, the rms perturbations are 740 ns and 5.0 μ s, respectively. Note that the predicted structure function extrapolated from $\Delta t_{\rm d}$ as given above, using the value of $\Delta t_{\rm d}$ estimated from scintillation measurements, is actually lower (by a factor of 5) than what is empirically estimated from the DM time series by Keith et al. (2013). This could potentially arise from additional structures in the interstellar medium, unrelated to general turbulence (Lam et al. 2016b).

2.1.3. Additional Sources of Uncertainty

Gancio et al. (2020) discuss the RFI environment around the observatory, including the amplitude and approximate impact on the pulsar observations. While the effect appears to be minimal, RFI is a growing concern at all observatories worldwide. IAR's proximity to the urban center of Buenos Aires means that active real-time mitigation will need to be implemented in the future to reduce any growing impact on the error budget. Also, importantly for the IAR Observatory, polarization miscalibration can be a significant contribution to the timing uncertainty, including when both polarizations are measured. Gancio et al. (2020) discuss the development of current and future polarization calibration routines as a goal for the IAR.

In addition to the TOA uncertainty estimates, PSR J0437 –4715 is known to show red noise in its timing residuals (e.g., Kerr et al. 2020), consistent with rotational spin noise (Shannon & Cordes 2010; Lam et al. 2017). While red noise will impact the sensitivity toward CWs, the use of matched filtering in detection analyses, coupled with the requirement to observe a correlated signal in multiple pulsars, means that individual red noise is of less critical significance in CW analyses versus stochastic-background analyses. In other words, while red noise can mimic the low-frequency time-correlated signal of the stochastic-background, detectable single sources are necessarily expected to be resolvable from

Again note that Equation (9) describes the rms fluctuations over a timescale τ rather than the full rms, which can be obtained by relating the structure function to the power spectrum of the timing perturbations (Lam et al. 2016b) and integrating to find the total variance.

within red noise. In particular, at frequencies larger than $\sim\!10\,\text{nHz}$, steep red noise does not affect CW sensitivity. This was explored in Xin et al. (2020) where the addition of red noise with a steep spectral index, there in the form of a gravitational wave background, had little effect at frequencies $>\!10\,\text{nHz}$. Strong red noise obviously can affect sensitivity, but this is highly dependent on the spectral index. Finally, at least some of PSR J0437–4715's red noise appears to be due to time-correlated noise in various receiver–backend combinations at Parkes (Lentati et al. 2016; Goncharov et al. 2021). Observations from various telescopes allow for the mitigation of these noise sources and more accurate characterization of the intrinsic red noise.

2.2. Pulsar GW Sensitivities

GW detection relies on measuring the signature of TOA perturbations among pulsars. In the case of a stochastic background—for instance, from the unresolvable sum of signals from SMBHBs—one relies on cross-correlations between these perturbations. For individual SMBHBs and other single-source signals, one uses a deterministic model. In both cases, the sky location and sensitivity of individual pulsars affect the ability of the full PTA to detect gravitational waves. We use the framework discussed in Hazboun et al. (2019) and Lam (2018) to estimate the sensitivity to single sources, which we describe here briefly.

While the ability to claim a detection of GWs from a single SMBHB requires more than one pulsar, the sensitivity to a single source depends on the signal strength and noise in each individual pulsar. These signals are then added up across the network to build a robust detection. There are a number of statistics defined in the literature to search for single-source GWs (Babak & Sesana 2012; Ellis et al. 2012a, 2012b; Taylor et al. 2016). Here, we focus on assessing and optimizing the sensitivity of PTAs (Lam 2018; Hazboun et al. 2019) given different pulsars and changes in the observing strategies. The framework of Hazboun et al. (2019) uses a matched-filter statistic tailored to studying sky-dependent sensitivity. The S/N, $\rho(\hat{k})$, is dependent on the response of an individual pulsar's sky position and noise characteristics, but has been averaged over inclination angle and GW polarization:

$$\langle \rho^2(\hat{k}) \rangle_{\text{inc}} = 2T_{\text{obs}} \int_{f_{\text{L}}}^{f_{\text{H}}} df \sum_{i} \frac{4}{5} \frac{T_i}{T_{\text{obs}}} \frac{S_h(f)}{S_i(f, \hat{k})}.$$
 (11)

Here, $S_h(f)$ is the strain power spectral density (PSD) of a monochromatic SMBHB signal, $T_i/T_{\rm obs}$ is the fraction of total observation time for the PTA covered by a particular pulsar labeled by i, and $S_i(f, \hat{k})$ is the strain-noise PSD for a particular pulsar. The dependence on sky location, \hat{k} , comes from the quadrupolar response function of pulsars to GWs. This S/N shows that the signals from individual pulsars add independently, but this really only tells part of the story. While the quantity $\rho(\hat{k})$ captures the sensitivity of a PTA to individual sources, one would need a significant signal in a few pulsars in order to claim a detection.

The PSD $S_i(f, \hat{k})$ is related to the usual noise spectra, written in Lam (2018) as the sum of white noise, red noise, and the stochastic GW background,

$$P_i(f) = P_{W,i}(f) + P_{R,i}(f) + P_{SB}(f),$$
 (12)

where the stochastic background term takes a power-law form of $P_{\rm SB}(f) \propto f^{-\beta}$ with $\beta=13/3$ for an ensemble of SMBHBs (Jenet et al. 2006). The PSD $S_i(f,\hat{k})$ also takes into account the timing model fit of the pulsar, through the inverse noise-weighted transmission function and the response function, which maps the strain from the GWs to the induced residuals in the pulsar's TOAs. See Hazboun et al. (2019) for more details. For uniform white noise given by $\sigma_{\rm W,i}$ between observations with cadence c_i , the white noise term is simply $P_{\rm W,i}(f)=2\sigma_{\rm W,i}^2/c_i$. This form demonstrates the strength of the IAR Observatory in observing PSR J0437–4715: the cadence can be a factor of \sim 30 larger than for other telescopes, thus significantly reducing the white noise term.

The strain power spectrum for a single CW source with GW frequency f_0 and amplitude h_0 is (Thrane & Romano 2013; Lam 2018; Hazboun et al. 2019)

$$S_h(f) \equiv \frac{1}{2} h_0^2 [\delta_T(f - f_0) + \delta_T(f + f_0)]. \tag{13}$$

where $\delta_T(f)$ is the finite-time approximating function of a Dirac delta function,

$$\delta_T(f) \equiv \frac{\sin(\pi f T)}{\pi f}, \quad \lim_{T \to \infty} \delta_T(f) = \delta(f).$$
 (14)

That is, given the simple CW approximation often used in PTA analyses of an unchanging orbital frequency, over an infinite time, the power spectrum would be a delta function at f_0 . While more realistic signals, such as those that include a phase shift from the delayed pulsar term and frequency evolution, are usually used in real PTA analyses (e.g., Aggarwal et al. 2019), the sensitivity is accurately estimated with a circular model. Additionally, it should be noted that this framework includes the signal from the time-delayed pulsar term. An analysis using the pulsar term requires very accurate pulsar distances in order to gain an appreciable signal; perfect knowledge of the distance boosts the squared S/N by a factor of 2. While standard analyses (Aggarwal et al. 2019) use the pulsar term, it is unclear how much is gained by its inclusion. This has no effect on the ratios of detection thresholds examined here, because the factor (of $\sqrt{2}$) for thresholds would cancel.

3. Current IAR Sensitivity of PSR J0437-4715

Here, we describe the current status of the observation of PSR J0437–4715 by the IAR. Observational and derived parameters for PSR J0437–4715 are provided in Table 2. Gancio et al. (2020) demonstrated 88 high-precision timing measurements from A1 and 106 from A2 in its preliminary timing campaign in 2019.

We will assume a standardized phase bin resolution of $N_{\phi}=512$. This choice implies that comparisons of pulse S/N will vary between observing setups (NANOGrav uses a uniform 2048, but other groups use variable values), though the TOA uncertainty will still be constant (Lam et al. 2016a). However, a uniform definition of pulse S/N, as in Equation (1), will allow us to project the sensitivity of the IAR observations more easily, and therefore it is still useful to convert between the two quantities $\sigma_{\rm S/N}$ and S.

Using the smoothed S/N-weighted average 20 cm template from the Parkes Pulsar Timing Array (PPTA; Kerr et al. 2020), we calculated the effective width $W_{\rm eff}$ of PSR J0437-4715 to be 667.6 μ s (see Table 2). From the residuals in Gancio et al. (2020), we calculated the median template-fitting uncertainties to be 200 and 325 ns for A1 and A2, respectively. With $N_{\phi} = 512$, the equivalent median S/N for A1 is 148.8, while that for A2 is 90.6. These values are consistent with those derived in Sosa Fiscella et al. (2021), who analyze an extended IAR data set. The differences in the S/N between both telescopes is not fully explained by the gain differences from dish materials nor differences in observation lengths. Insertion losses are slightly higher for A2, which may additionally account for some of the S/N difference. We use the parameter values given above to form the basis of our extrapolation to future observing configurations in the next section, noting that they may be conservative estimates such that the performance of A2 on the frontend may improve in the future more than our naive scalings would suggest.

4. Extrapolation of IAR Observations of PSR J0437-4715 to Future Systems

In this section, we provide estimates of the IAR's sensitivity with changes in the observing configuration, namely the use of different receiver ranges for the two antennas. We also compare with sensitivity estimates of other facilities observing PSR J0437–4715 and show that the IAR's substantial cadence, i.e., its time on the source, will provide it with a special capability to observe this pulsar in the future.

4.1. Upgraded Observing Configurations

To estimate the TOA uncertainties for each system, we combined the various noise components in the following manner. We scaled the A1 and A2 median S/Ns as estimated in Section 3, and scale by the ratio of the flux densities from 1400 MHz to the new center frequency, the ratio of the square root of the bandwidths and number of polarization channels, and inversely by the ratio of the receiver temperatures. With the new S/N, we calculated a new template fitting error for the receiver. With the two center frequencies, we were able to calculate the TOA uncertainty due to DM estimation (Equation (6)); we assumed that, in all future timing analyses, DM will be estimated on a time-varying basis such that the rms timing fluctuations are negligible (e.g., from Equation (9)), otherwise the unmodeled DM variations will make any highprecision timing experiment impossible. Last, we added in 100 ns of uncertainty due to polarization miscalibration, comparable to the value calculated by van Straten (2006).

Even though we approximated the observations across each band as single measurements, ignoring the varying spectral index with the band, changes in pulse width, etc., for simplicity we calculated the TOA uncertainties as if there are two "spot" measurements at each center frequency. While this is a simplification, it provided us with a *conservative* estimate, since a full least-squares fit formalism will lead to reduced TOA uncertainties.

In summary, our TOA uncertainties consisted of template fitting errors, DM estimation errors, and polarization miscalibration errors, added together in quadrature.

We considered several different configurations: both the current and future setups as described in Gancio et al. (2020),

as well as setups where additional receivers are built. We restricted ourselves to discussing the configurations broadly, assuming that the receiver frontend is matched with a backend that will be able to adequately sample and coherently dedisperse the data. Gancio et al. (2020) describe the future planned upgrades to the antennas, which include receivers reaching system temperatures $T_{\rm sys}$ < 50 K, a 500 MHz bandwidth in a range between 1 and 2 GHz, and a new FPGA-based CASPER board (Hickish et al. 2016) backend capable of processing the increased bandwidth. For other configurations we list, we assumed similar matching, as we primarily wanted to focus on estimating the TOA uncertainties given the assumed development of a specific system. We estimated these uncertainties under two scenarios with the current equipment: three in which one or more of these higherbandwidth systems is deployed, and one optimistic scenario in which ultrawideband receivers are deployed on both antennas. The full list of assumptions is provided in Table 3, along with the TOA uncertainties we estimate. The gains of the antennas in our analysis did not vary, though some dish or efficiency improvements may be possible in the future, e.g., resurfacing the dishes in the future may improve the aperture efficiencies slightly as compared with their current materials (Testori et al. 2001: Gancio et al. 2020).

We describe the rationales for considering each configuration below.

- C1: Current. This configuration is as described in Gancio et al. (2020); see their Table 1.
- C2: Optimized. Since the center frequencies are tunable, we allowed for the maximum separation in frequencies, to minimize TOA uncertainties from DM misestimation. We also halved A1's bandwidth coverage in favor of dual-polarization measurements (see their Section 2.1 regarding these two modes for A1), a requirement for high-precision timing.
- C3: Wideband. With a modest upgrade of two receivers and backends covering 500 MHz each, as discussed in Gancio et al. (2020), the two antennas can cover the 1–2 GHz range. The target system temperature is $T_{\rm sys} < 50$ K. While some parts of the band will be lost due to RFI, no significant segments of the band are currently lost across this frequency range (Gancio et al. 2020).
- C4: Low Frequency. Instead of two receivers covering the full L-band range, we instead selected one 500 MHz receiver to cover the top end of L band $(1.5-2.0 \,\mathrm{GHz})$ for A1, and then for A2 considered a receiver from 400-450 MHz. This lower frequency range is used by NANOGrav at Arecibo for some pulsars. Its primary allocation in Argentina is for maritime communication and radionavigation (see ITU-R 2016 for Region 2), which helps to limit fixed sources of RFI. In addition, scattering will minimally affect PSR J0437-4715, given its low DM, and so the increased flux density (see Table 2) can lead to high-S/N TOAs, also providing a significant frequency difference to estimate DM. For the L-band receiver, we used the higher end of the possible bandwidth range in order to minimize TOA uncertainties due to DM misestimation.

⁵ Ente Nacional de Comunicaciones (ENACOM) follows ITU-R regulations, as described in Ente Nacional de Comunicaciones (2019).

 Table 3

 Observing Configurations for the IAR Antennas

Parameter	C1: Current		C2: Optimized		C3: Wideband		C4: Low Freq		C5: High Freq		C6: Dual UWB	
	A1	A2	A1	A2	A1	A2	A1	A2	A1	A2	A1	A2
Circular Polarizations (N _{pol})	1	2	2	2	2	2	2	2	2	2	2	2
Center Frequency (ν_0 , MHz)	1400	1400	1128	1572	1750	1250	1750	425	2500	1250	1200	1200
Bandwidth (B, MHz)	112	56	56	56	500	500	500	50	500	500	1600	1600
Receiver Temperature (T_{rcvr}, K)	100	110	100	110	50	50	50	50	50	50	50	50
$Gain (G, K Jy^{-1})$	0.084	0.077	0.084	0.077	0.084	0.077	0.084	0.077	0.084	0.077	0.084	0.077
PSR J0437–4715 TOA Uncertainty ($\sigma_{\rm eff}$, μ s)	2.9	95	2.	31	0.	46	0.	34	0.	36	0.	19

Note. Current (C1) configuration values are taken from Gancio et al. (2020); see their Table 1. We have defined the system gain in terms of K Jy⁻¹, the "forward" gain, with values of 1/G instead given in Gancio et al. (2020) and Table 2. The maximum tracking time (T_{obs}) for both antennas is 3^h 40^m, and we assume observations are performed at a daily cadence.

C5: High Frequency. As a parallel to C4, we considered instead using a second receiver at higher frequencies, in the 2.5 GHz (*S* band) range, which is also used by NANOGrav at Arecibo for some pulsars. This region of the frequency spectrum often contains significant RFI due to overlap with wireless communications. Nonetheless, we considered the potential for such a system. For the *L*-band receiver, we used the lower end of the possible bandwidth range in order to minimize TOA uncertainties due to DM misestimation.

C6: Dual Ultrawideband. As an optimistic setup, we considered the receiver systems as described in Hallinan et al. (2019) for the DSA-2000. This observatory will employ low-cost receiver systems from 0.4–2.0 GHz for each of its 2000 antennas. While their target system temperature is 25 K, we kept 50 K for use in this considered configuration. Since the receiver setup is identical for both antennas, for simplicity we assumed two bands centered at 700 and 1500 MHz with 600 and 1000 MHz of bandwidth, respectively, to cover the 400–2000 MHz range, and included a factor of √2 in our calculation.

As discussed in Section 2.1.1, one astrophysical cause of the S/N changing is diffractive scintillation. When considering wider bandwidths, the number of scintles will grow, thus causing the pulse S/N to tend more toward a mean value rather than covering an exponentially distributed range. In practice, this means that, for low-bandwidth setups such as the current configurations, there are epochs in which the template fitting error in Equation (1) breaks down (Arzoumanian et al. 2015) and TOAs cannot be reliably estimated, resulting in a loss of usable data. In addition to the mean S/N S_0 increasing due to wider bandwidths, the change in the diffractive scintillation PDF means that the TOAs will tend toward higher mean/median values, without a loss of data. Thus, we considered the extrapolation from the median S/N in Section 3 to be more robust.

For our analysis, we assumed that configurations C3 through C6 are operational by 2023, a rapid timeline, and assumed that the observing conditions are static into the future. As with all facilities, future upgrades may yield additional sensitivity. In addition, growing RFI will impact timing sensitivity as well. Gancio et al. (2020) show that $\sim 10\%$ of observing times are significantly affected due to RFI, with significantly less time at night. RFI affects both antennas differently, given their differing proximities to the local IAR offices. The RFI tends

to be narrowband, and thus can be excised while retaining the majority of the band. In our work, we ignored the role of RFI, noting that it will play an important but small role in the assumptions we are making, regardless.

4.2. Comparison with Other Observatories

Using the single-pulsar-dependent terms in Equation (11) and the instrumental/telescope-dependent components of the TOA uncertainty, defined below, we constructed a metric that describes the overall timing precision of a pulsar in an array (with the subscript i being dropped):

$$M \equiv \left(\frac{Tc}{\sigma_{\rm eff}^2}\right)^{1/2} = 34.6 \ \mu \rm s^{-1} \left(\frac{T}{10 \ \rm yr}\right)^{1/2} \left(\frac{c}{12 \ \rm yr^{-1}}\right)^{1/2} \times \left(\frac{\sigma_{\rm eff}}{0.1 \ \mu \rm s}\right)^{-1}.$$
 (15)

When T is the total observing baseline in years, c is the observing cadence in years⁻¹, and $\sigma_{\rm eff}$ is the *effective* telescope-dependent TOA uncertainty in μ s, then M_i has units of μ s⁻¹. We define $\sigma_{\rm eff}$ here as the combination (quadrature sum) of the short-timescale white noise, the DM estimation uncertainty due to the white noise (Equation (6)), and polarization calibration uncertainty (taken to be 100 ns; see Section 4.1. The short-timescale white noise includes template-fitting, jitter, and scintillation-noise uncertainties. As discussed in Section 2, jitter becomes negligible for the duration of observations conducted by the IAR, but not necessarily for other observatories. Scintillation noise is negligible, given the small scattering timescale.

The quantity *M* acts like a signal-to-noise ratio, where larger *M* implies a higher sensitivity, though we note that it is not a direct relationship. Alternatively, this quantity can be viewed as proportional to the (square) inverse of the error on the mean of the residuals.

Figure 1 shows curves of M as a function of time for a number of different telescopes and configurations. The three blue curves denote three different IAR configurations as listed in Table 3, where we take the start time for C2 to be mid-2020, and we assume an aggressive program start time of 2023 January for all other upgraded configurations. Delays will shift the curves to the right. Nonetheless, it is quite clear how drastically instrumentation improvements can improve M.

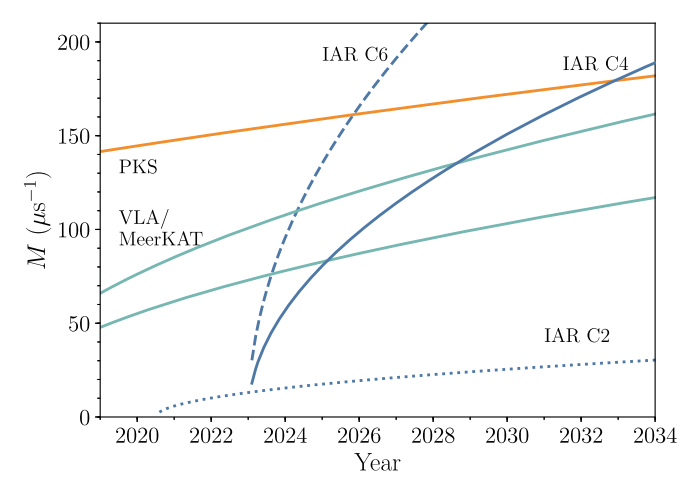


Figure 1. Plots of the timing precision metric M (see Equation (15)) vs. time. Increased M implies improved sensitivity. Blue lines denote the various IAR configurations, where C4 and C6 start in 2023. Metric for Parkes is shown in orange, and the two teal curves show the metric for the VLA /MeerKAT assuming two different estimates for polarization noise.

Comparisons to other observatories are described in the following subsections.

4.2.1. The Parkes Telescope

The PPTA has observed PSR J0437–4715 since 1996 (Hobbs 2013), with a typical cadence of once every two weeks in three bands (Manchester et al. 2013; Reardon et al. 2016; Kerr et al. 2020) for approximately one hour in each of the 20 (1400 MHz) and $10/50 \, \mathrm{cm}$ ($3100/730 \, \mathrm{MHz}$) observations (Hobbs 2013). The backend systems have improved over time, resulting in many different noise contributions to consider. We estimated the equivalent σ_{eff} as follows. Using the PPTA Second Data Release⁶ (Kerr et al. 2020), we used the empirically derived noise parameters as an estimate for the telescope-dependent σ_{eff} described previously.

First, we took parameters that describe modifications to the template-fitting uncertainties, namely a noise added in quadrature (EQUAD) with the resultant quantity multiplied by a scaling factor (EFAC), to provide us with an estimate of the white noise for each TOA (Reardon et al. 2016). Since the white noise parameters in Kerr et al. (2020) were derived from subbanded TOAs, i.e., those taken from small frequency channels over a wider bandwidth, we then computed the epochaveraged error as in Lam et al. (2018; see also references therein), to provide us with the amount of white noise per epoch per band. This amounts to computing the square root of $(U^TC^{-1}U)^{-1}$, where U is a column matrix of ones and C is the covariance matrix, which in this case is a diagonal matrix containing the squared of the modified TOA uncertainties.

These epoch-averaged TOA uncertainties describe the measured white noise in the Kerr et al. (2020) data set. We also included the measured "band noise" terms, which describe additional noise as a function of specific frequency ranges. Such band noise can describe either additional chromatic propagation effects or terrestrial effects such as from RFI or polarization miscalibration (Lentati et al. 2016). Recall that we argued in Section 2 that PSR J0437–4715 likely has low levels of noise due to unmodeled propagation effects such as scattering. Therefore, we took the band noise to be due to

terrestrial effects, and as such, we consider it to be an important contribution to σ_{eff} . To add a band noise component to the TOA uncertainties, we determined the variance numerically by integrating the power-law spectrum form described by the amplitude and index parameters (values set by the parameter TNBandNoise in the data files). These variances were added to the white noise variance per epoch per band computed above to appropriately adjust the uncertainties. Finally, to use a single number to project M to, we computed the average "weight" of each uncertainty ($w_k = 1/\sigma_k^2$ for the kth TOA), computed the mean weight, and then calculated the square root of reciprocal of this mean weight. Our end result was $\sigma_{\rm eff} = 166$ ns. In our sensitivity extrapolation calculation, we did not account for any remaining variance in the timing residuals, e.g., due to DM estimation or improper polarization calibration, which we assumed in our analysis was accounted for elsewhere in the original noise modeling of the data set.

We note that an ultrawideband receiver system has been deployed at Parkes (Hobbs et al. 2020), which may result in reduced uncertainties in the future if RFI does not become sufficiently problematic. If so, this will improve future estimates of M for Parkes as compared with what is shown in Figure 1. However, the majority of the amplitude of M comes from the large observing baseline T more so than the TOA uncertainty, so it is unclear by how much M will be affected.

4.2.2. The Very Large Array

NANOGrav has also begun⁷ a program to observe PSR J0437–4715 with the VLA monthly between 1 and 4 GHz, with 30 total minutes devoted to *L* band (1–2 GHz) and 30 minutes devoted to *S* band (2–4 GHz). While the full hour includes overhead time, for the purposes of our calculations, we will assume each observation is 30 minutes long.

Without empirically derived white noise parameters as in the PPTA data release, while we could work out a full calculation of the white noise plus DM uncertainties, we will instead provide a heuristic argument to demonstrate that the observational setup with the VLA will result in a lower M. Let us assume that jitter is the only white noise contribution to the TOA uncertainty. Using the values in Shannon et al. (2014; see also Table 2), we have that the rms jitter for a 1 hr observation is 48 ns at L band and 41 ns at S band. Given that jitter scales as the square root of the number of pulses, the 30 minute rms jitter will be 68 and 58 ns for the two bands, respectively. For DM estimation errors, we will assume for this argument that the two spot frequencies are 1 and 4 GHz rather than center frequencies of 1.5 and 3 GHz, which will underestimate the uncertainty but will not matter for a comparison. Using our assumed numbers, calculating $\sigma_{\widehat{DM}}$ using Equation (6), and then finding the total infinite-frequency TOA uncertainty, we have 76 ns per observation as a minimum bound. With observations starting in 2016, and assuming 12 observations per year continued until 2033, we have M between 123 and $170 \,\mu\text{s}^{-1}$, assuming 50 and 100 ns of polarization calibration uncertainty, respectively.

4.2.3. MeerKAT

MeerKAT has begun pulsar-timing observations with the MeerTime project (Johnston et al. 2020; Bailes et al. 2020), with one goal of the project being to observe MSPs. With the

Files are available at doi:10.25919/5db90a8bdeb59.

Proposal IDs VLA/16B-240, VLA/18A-210, VLA/19A-356.

expected next generation of receivers extending the observatory's bandwidth range, in a subarray mode, MeerKAT will be able to observe from 0.9–3.5 GHz (Bailes et al. 2018, 2020). If we again assume that the pulsar is jitter-dominated, as with the VLA, then we expect comparable numbers as calculated above.

4.2.4. Comparing M for Different Observatories

Figure 1 shows M for the VLA (again, comparable with MeerKAT), Parkes (PKS), and three configurations for the IAR: C2, C4, and C6. Given the assumptions presented above, we see that an aggressive timeline for improved instrumentation will drastically improve IAR's sensitivity to PSR J0437 -4715 in comparison to other facilities. Delays in this timeline will shift the curve to the right, but the conclusion remains the same: a modestly upgraded IAR facility (C4) will drastically aid in single-source GW science right in the era of the first CW sources, as well as the first observations by LISA. Using stateof-the-art yet low-cost instrumentation (e.g., C6 using similar instrumentation as described in Hallinan et al. (2019)) will provide the IAR with unparalleled sensitivity to PSR J0437 -4715, and thus make it a unique contributor to GW science with PTAs by the middle to end of the current decade. We note that other observatories like Parkes are complementary for long-timescale (~decade) GW periods, given that its observations of PSR J0437-4715 cover a sufficient number of cycles whereas observations by the IAR alone will not.

5. GW Projections for PSR J0437-4715

In order to demonstrate the usefulness of PSR J0437–4715 as an addition to the NANOGrav observing campaign, we projected the status of the PTA described in Arzoumanian et al. (2018b) into the next decade. Here, we are only interested in how PSR J0437–4715 contributes to the sensitivity for deterministic signals, so we simply extended the baselines of the data set most recently used in these GW analyses, using the noise characteristics and sky locations of the current set of pulsars and those estimated for PSR J0437–4715 at IAR. We only investigated single-source sensitivity because (1) the GWB is forecasted to be detected long before the dates of these projections and (2) the short baseline of PSR J0437–4715 when it is added to NANOGrav data sets will not be very useful for detection/characterization of the GWB until it has sensitivity at lower frequencies.

Using the Python package hasasia (Hazboun et al. 2019), we simulated a PTA with the same characteristics as Arzoumanian et al. (2018b) but added 17 yr of data to use as a baseline for our comparison, ending in 2033. We used the noise models/parameters laid out in Arzoumanian et al. (2018b), including the measured TOA residual rms values, and where significantly measured, red noise as well. These models estimate various white noise contributions, mismodeled chromatic effects and intrinsic spin noise. We also simulated two versions of a PTA with IAR observations of PSR J0437 -4715 from 2023 onward, i.e., 10 yr of observations. Similarly, we used a total residual rms value and red noise parameters, given in Kerr et al. (2020). In particular, we added red noise with $\log_{10} A_{\rm RN}(f_{\rm vr}) = -14.0186$ and spectral index of $\gamma = 3.17$. The two versions correspond to using configurations C4 and C6.

Figure 2 shows the ratio of the sky sensitivity in source strain (see Equation (80) in Hazboun et al. 2019) when adding

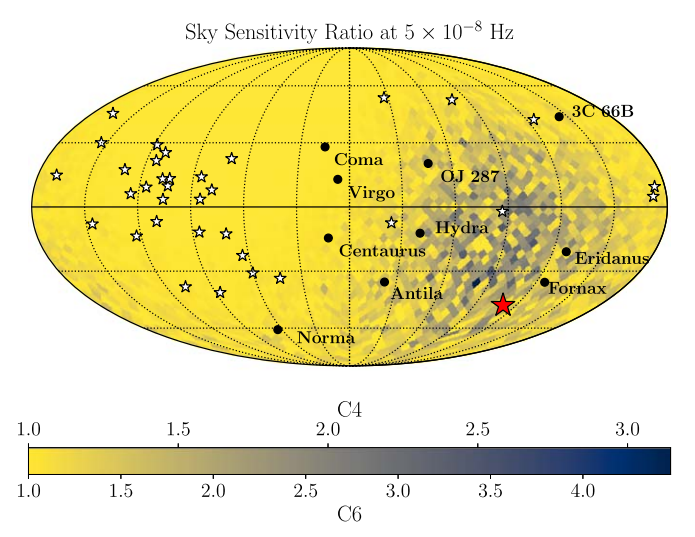


Figure 2. Ratio of the GW sensitivity when adding PSR J0437–4715 to the PTA using configurations C4 and C6 vs. otherwise. Sensitivity is calculated at 5×10^{-8} Hz. NANOGrav 11 yr data set pulsars are shown as white stars, and PSR J0437–4715 as the red star. Possible targets of interest for CW signals are shown as the black dots and labeled accordingly. Equatorial coordinates are shown, with R.A. increasing to the left every $2^{\rm h}$ starting from the right and decl. increasing upward every 30°. Structure of the sky map is the same for C4 and C6, but the corresponding color map scale is shown at the bottom for each. We see clear, significant increases to the sensitivity in NANOGrav's current "blind spot" on the sky, due to the addition of PSR J0437–4715.

observations of PSR J0437–4715 versus not. We show the positions of the NANOGrav 11 year data set pulsars (white stars), PSR J0437–4715 (red star), and nearby galaxy clusters and individual targets of interest (e.g., Mingarelli et al. 2017; Chen & Zhang 2018; Aggarwal et al. 2019; Arzoumanian et al. 2020). We used a GW frequency of 5×10^{-8} Hz to highlight where the observations of PSR J0437–4715 make a sizable impact on the sensitivity. The sky maps are identical in structure, but the overall sensitivity varies when using C4 versus C6. At a frequency of 10^{-8} Hz, approximately where the current most sensitive CW upper limits are (Aggarwal et al. 2019), the increase in source strain is only about 15%, while at 10^{-9} Hz, any increase in sensitivity is negligible. This dependence on frequency is due in part to the sizable amount of red noise in the TOAs of PSR J0437–4715.

We see clear indications that observations with PSR J0437 -4715 versus without will increase the sensitivity of the NANOGrav PTA. In the case of C6, by 2033 the array's sensitivity improves by a factor of \approx 2–4.5 for 20% of the sky. Even with C4, the improvement ratio is \approx 1.4–3. Since the observed GW strain is inversely proportional to the distance of a source, a factor of 2 increase in sensitivity leads to the array being able to search out a factor of 2 in distance, indicating that the volume NANOGrav will be able to probe in its current "blind spot" will be drastically increased.

6. Predictions for Observations of Other MSPs

Our estimates and extrapolations for PSR J0437–4715 can be used to predict the general timing performance of other pulsars observable with the IAR. While PSR J0437–4715 is the brightest known MSP, other factors influence the overall timing precision. Table 4 provides a list of some pulsars observed by the PPTA (Kerr et al. 2020), which we use as a representative list to quantify potential targets.

PSR	P (ms)	DM (pc cm ⁻³)	W ₅₀ (μs)	W ₅₀ /P (%)	$W_{ m eff} \ (\mu m s)$	$ar{U}_{ m obs}$	<i>I</i> ₁₄₀₀ (mJy)	R
J0437-4715	5.76	2.6	141.8	2.5%	667.6	0.063	158.0	1.000
J1017-7156	2.34	94.2	72.0	3.1%	292.6	0.036	0.9	0.022
J1125-6014	2.63	53.0	131.6	5.0%	257.1	0.073	0.9	0.013
J1600-3053	3.60	52.3	92.7	2.6%	469.3	0.051	2.5	0.028
J1603-7202	14.84	38.0	316.2	2.1%	1480.7	0.060	3.5	0.010
J1643-1224	4.62	62.4	318.6	6.9%	978.7	0.098	4.7	0.013
J1730-2304	8.12	9.6	573.1	7.1%	891.5	0.109	3.8	0.010
J1744-1134	4.07	3.1	137.7	3.4%	512.2	0.037	2.5	0.035
J1909-3744	2.95	10.4	43.8	1.5%	266.2	0.017	1.7	0.100
J2241-5236	2.19	11.4	64.3	2.9%	248.3	0.033	1.8	0.058

Table 4Predicted Sensitivity of Other Observable MSPs

For the same observational setup, we expect that the period-averaged signal-to-noise ratio \bar{S} will be proportional to the period-averaged flux density I_0 at a fiducial frequency ν_0 , using the notation of Lam et al. (2018). Wide-bandwidth observations require that the spectral index of the pulsar flux be considered. In general, the minimum TOA uncertainty due to a finite S/N is given by Equation (1), which uses the peak-to-off-pulse S/N, S. The conversion between the two is given by $\bar{S} = \bar{U}_{\rm obs} S$, where

$$\bar{U}_{\text{obs}} = \frac{1}{N_{\phi}} \sum_{i=0}^{N_{\phi}-1} U_{\text{obs}}(\phi_i)$$
 (16)

is the mean value of the template shape $U_{\rm obs}$. A smaller value of $\bar{U}_{\rm obs}$ implies a sharper pulse profile, which yields improved TOA uncertainties. Therefore, combining the pulse-shape-dependent factors with the pulsar fluxes, we can relate the ratio of the template-fitting uncertainties between two pulsars A and B as

$$R \equiv \frac{\sigma_{\text{S/N, A}}}{\sigma_{\text{S/N, B}}} = \frac{W_{\text{eff, A}}\bar{U}_{\text{obs, A}}/I_{0, A}}{W_{\text{eff, B}}\bar{U}_{\text{obs, B}}/I_{0, B}}.$$
(17)

With Equation (17), we were able to calculate the template fitting errors for the pulsars provided in Table 4 compared to PSR J0437–4715. In the table, the larger R is, the better the template fitting uncertainty will be. This analysis does not take into account other sources of uncertainty in TOA estimation. For example, sources with higher DM are more likely to be affected by pulse broadening due to interstellar scattering (Bhat et al. 2004). In addition, Equation (17) also does not take into account the decl. dependence of the tracking times of the antennas, which will introduce a $T_{\rm obs}$ dependence affecting the S/N for each pulsar.

We can more intuitively understand the impact of the pulse shape metrics compared to the flux densities in Equation (17) by considering a Gaussian-shaped pulse. The effective width $W_{\rm eff} \propto (W_{50}P)^{1/2}$, the geometric mean of the pulse full width at half maximum W_{50} and the pulse period P (following from Equation (2); see also Lam et al. (2016a)). In considering a Gaussian pulse, the mean value of the pulse will be the integral of the pulse shape divided by the pulse period, yielding the approximate relationship $\bar{U}_{\rm obs} \propto W_{50}/P$ for sufficiently narrow pulses. Combining these, we have

$$W_{\rm eff} \, \bar{U}_{\rm obs} \propto (W_{50} P)^{1/2} \frac{W_{50}}{P} = P \left(\frac{W_{50}}{P}\right)^{3/2}.$$
 (18)

We write the second equality in terms of the pulse duty cycle, W_{50}/P . We see from Equation (18) that decreases in either the pulse period or the duty cycle will lead to a lower $\sigma_{\rm S/N}$, which is to be expected. These improvements can help compensate for a difference between the flux densities of pulsars. A factor of two decrease in both the pulse period and duty cycle can then offset a factor of five decrease in the flux density of one pulsar compared to another and lead to equivalent $\sigma_{\rm S/N}$. Note that, in comparison to PSR J0437–4715, decreases in P or W_{50}/P by more than a factor of \sim 2 are generally not observed.

Table 4 gives the various pulse shape parameters for ten pulsars observed by the PPTA in the decl. range of IAR and with R > 0.01. Pulse shape metrics were measured using the 20 cm Parkes Digital Filterbank System 4 (PDFB4) templates⁸ in Kerr et al. (2020). We used the median flux density at 1400 MHz reported by Kerr et al. (2020) in our analysis; the scintillation properties of the different pulsars will affect R, but we ignored that here and only considered a typical observation. From these measurements, we calculated R according to Equation (17).

Another pulsar with one of the lowest DMs, PSR J1744 -1134, has been detected by the IAR in individual observations (L. Combi 2021, private communication). As with PSR J0437-4715, we can then consider the impact of daily cadence using the IAR compared with ~monthly observations available at other facilities. Let us naively consider PSR J0437 -4715 observed with $\sigma_{\rm eff} \approx \sigma_{\rm S/N} = 200$ ns. While R = 0.035for PSR J1744-1134, leading to many microseconds of uncertainty per epoch, the monthly averaged uncertainty reduces by a factor of $\sqrt{30}$ to approximately 1 μ s. This argument ignores differences in spectral index, differences in $T_{\rm obs}$ due to the decl., and other frequency-dependent profile changes, but serves to demonstrate the potential of IAR's capabilities. The sensitivity of observations of PSR J1744 -1134 with daily cadence will be comparable to those of other pulsars with microsecond timing observed with a monthly cadence, making observations of the pulsar of sufficient quality for PTA science. Several other possible targets, such as PSRs J1909-3744, J2241-5236, and possibly also J1600 -3053, may be suitable candidates for daily monitoring.

7. Concluding Remarks

The IAR's special capabilities to observe PSR J0437-4715 will lead to a significant increase in CW sensitivity for PTAs.

Accessible at doi:10.25919/5db90a8bdeb59.

Several other 30 m class telescopes exist in the Southern Hemisphere: for example, the Hartebeesthoek Radio Astronomy Observatory (HartRAO; Chukwude 2007) and Mount Pleasant Radio Observatory (Dodson et al. 2007) have already been used for long-term pulsar observations, and in Argentina, the European Space Agency's Deep Space Antenna 3 tracking station (Benaglia et al. 2011) and the joint Argentina-China deep space network antenna CLTC-CONAE-NEUQUÉN (Colazo et al. 2020) will complement the IAR with dedicated time for national radio astronomy projects. In all cases, significant improvements to the instrumentation, e.g., increased bandwidths, would be required for obtaining high-precision TOA estimates of PSR J0437-4715. The IAR is currently specifically targeting high-precision pulsar timing as a goal science driver for its observatory. However, it is vital that the IAR observatory receives the necessary upgrades to make this a possibility; without dual-polarization observations at frequencies spaced widely enough to accurately estimate DM, the IAR will not be able to meet the target sensitivities described here. This will require careful polarization calibration, and the RFI environment around the observatory must remain in a clean

In addition to direct CW sensitivity, high-cadence observations can contribute to other PTA-related science. For example, daily monitoring of DMs and scintillation, which will feed back into understanding pulsar timing noise models, is a planned goal of the IAR (Gancio et al. 2020). Such observations will complement those of Northern Hemisphere facilities like CHIME ($\delta > -20^\circ$; Ng 2018), which are beginning to provide unprecedented measurements of the interstellar medium on short timescales (Ng et al. 2020). For example, given the proper motion of PSR J0437–4715 of 141 mas yr⁻¹ (Kerr et al. 2020) and distance of 156.8 pc, the pulsar's transverse velocity is 105 km s⁻¹. Over 10 yr of daily observations, the line of sight will probe length scales in the interstellar medium between 0.06–200 au.

International PTA efforts will also benefit from the inclusion of IAR observations. The International Pulsar Timing Array (IPTA) collaboration helps to coordinate these worldwide efforts, and while the potential target pulsars listed here would not be new additions to any future combined data set, such a data set will have improved sensitivity to GWs of all kinds with additional high-precision data. While Figure 1 shows the C4 or C6 configurations matching the sensitivity of Parkes on the timescale of years to a decade, combination of these data as part of the IPTA would yield the optimal results. High-cadence observations obtained by the IAR would complement the longer-term observations by Parkes to probe across GW frequencies. In addition, with the added sensitivities of other facilities performing new observations of PSR J0437-4715 and the sky coverage of all of the pulsars in the remainder of the combined IPTA data set, we can expect the IAR to be a significant contributor to GW science within even the next several years. Furthermore, uniform observations of several pulsars by the IAR could help constrain systematic variations between different frontend/backend systems for different telescopes, as well as between telescopes. For example, timing offsets or calibration errors could be detected, since a stable system could be compared against. Such observations could thus potentially reduce the overall noise of such a combined IPTA data set.

We thank Luciano Combi and the Pulsar Monitoring in Argentina (PuMA) for useful discussions in the preparation of this work. The NANOGrav Project receives support from NSF Physics Frontiers Center award No. 1430284. M.T.L. acknowledges support from NSF AAG award No. 2009468.

ORCID iDs

M. T. Lam https://orcid.org/0000-0003-0721-651X J. S. Hazboun https://orcid.org/0000-0003-2742-3321

References

Aggarwal, K., Arzoumanian, Z., Baker, P. T., et al. 2019, ApJ, 880, 116

```
Aggarwal, K., Arzoumanian, Z., Baker, P. T., et al. 2020, ApJ, 889, 38
Alam, M., Arzoumanian, Z., Baker, P. T., et al. 2021a, ApJS, 252, 4 Alam, M., Arzoumanian, Z., Baker, P. T., et al. 2021b, ApJS, 252, 5
Anholm, M., Ballmer, S., Creighton, J. D. E., Price, L. R., & Siemens, X. 2009,
   PhRvD, 79, 084030
Armstrong, J. W., Rickett, B. J., & Spangler, S. R. 1995, ApJ, 443, 209
Arzoumanian, Z., Baker, P. T., Brazier, A., et al. 2018a, ApJ, 859, 47
Arzoumanian, Z., Baker, P. T., Brazier, A., et al. 2020, ApJ, 900, 102
Arzoumanian, Z., Brazier, A., Burke-Spolaor, S., et al. 2015, ApJ, 813, 65
Arzoumanian, Z., Brazier, A., Burke-Spolaor, S., et al. 2018b, ApJS, 235, 37
Babak, S., & Sesana, A. 2012, PhRvD, 85, 044034
Bailes, M., Barr, E., Bhat, N. D. R., et al. 2018, arXiv:1803.07424
Bailes, M., Jameson, A., Abbate, F., et al. 2020, PASA, 37, e028
Benaglia, P., Casco, N., Cichowolski, S., et al. 2011, BAAA, 54, 447
Bhat, N. D. R., Cordes, J. M., Camilo, F., Nice, D. J., & Lorimer, D. R. 2004,
    pJ, 605, 759
Burt, B. J., Lommen, A. N., & Finn, L. S. 2011, ApJ, 730, 17
Chen, J.-W., & Zhang, Y. 2018, MNRAS, 481, 2249
Chukwude, A. E. 2007, ChJAA, 7, 521
Colazo, M., Gancio, G., & Command, H. 2020, BAAA, 61B, 228
Coles, W. A., Rickett, B. J., Gao, J. J., et al. 2010, ApJ, 717, 1206
Cordes, J. M., & Chernoff, D. F. 1997, ApJ, 482, 971
Cordes, J. M., Kramer, M., Lazio, T. J. W., et al. 2004, NewAR, 48, 1413
Cordes, J. M., & Rickett, B. J. 1998, ApJ, 507, 846
Cordes, J. M., & Shannon, R. M. 2010, arXiv:1010.3785
Cordes, J. M., Wolszczan, A., Dewey, R. J., Blaskiewicz, M., &
   Stinebring, D. R. 1990, ApJ, 349, 245
De, K., Gupta, Y., & Sharma, P. 2016, ApJL, 833, L10
Detweiler, S. 1979, ApJ, 234, 1100
Dodson, R., Lewis, D., & McCulloch, P. 2007, Ap&SS, 308, 585
Ellis, J. A., Jenet, F. A., & McLaughlin, M. A. 2012a, ApJ, 753, 96
Ellis, J. A., Siemens, X., & Creighton, J. D. E. 2012b, ApJ, 756, 175
Ente Nacional de Comunicaciones 2019, Cuadro de Atribución de Bandas de
   Frecuencias de la República Argentina (CABFRA; Table of Attribution of
   Frequency Bands of the Argentine Republic) (Buenos Aires, Argentina:
   ENACOM), https://www.enacom.gob.ar/cuadro-de-atribucion-de-bandas-
   de-frecuencias-de-la-republica-argentina-cabfra-_p1588
Foster, R. S., & Backer, D. C. 1990, ApJ, 361, 300
Foster, R. S., & Cordes, J. M. 1990, ApJ, 364, 123
Gancio, G., Lousto, C. O., Combi, L., et al. 2020, A&A, 633, A84
Goncharov, B., Reardon, D. J., Shannon, R. M., et al. 2021, MNRAS, 502, 478
Gwinn, C. R., Hirano, C., & Boldyrev, S. 2006, A&A, 453, 595
Hallinan, G., Ravi, V., Weinreb, S., et al. 2019, BAAS, 51, 255
Hazboun, J., Romano, J., & Smith, T. 2019, JOSS, 4, 1775
Hazboun, J. S., Romano, J. D., & Smith, T. L. 2019, PhRvD, 100, 104028
Hellings, R. W., & Downs, G. S. 1983, ApJL, 265, L39
Hickish, J., Abdurashidova, Z., Ali, Z., et al. 2016, JAI, 5, 1641001
Hobbs, G. 2013, CQGra, 30, 224007
Hobbs, G., Manchester, R. N., Dunning, A., et al. 2020, PASA, 37, e012
International Telecommunication Union Radiocommunication Sector (ITU-R)
   2016, Radio Regulations, Vol. I (Geneva: ITU)
Jenet, F. A., Hobbs, G. B., van Straten, W., et al. 2006, ApJ, 653, 1571
Johnston, S., Karastergiou, A., Keith, M. J., et al. 2020, MNRAS, 493, 3608
Johnston, S., Lorimer, D. R., Harrison, P. A., et al. 1993, Natur, 361, 613
Keith, M. J., Coles, W., Shannon, R. M., et al. 2013, MNRAS, 429, 2161
Kelley, L. Z., Blecha, L., Hernquist, L., et al. 2018, MNRAS, 477, 964
Kerr, M., Reardon, D. J., Hobbs, G., et al. 2020, PASA, 37, e020
Lam, M. T. 2018, ApJ, 868, 33
Lam, M. T., Cordes, J. M., Chatterjee, S., et al. 2016a, ApJ, 819, 155
Lam, M. T., Cordes, J. M., Chatterjee, S., et al. 2016b, ApJ, 821, 66
```

```
Lam, M. T., Cordes, J. M., Chatterjee, S., et al. 2017, ApJ, 834, 35
Lam, M. T., Lazio, T. J. W., Dolch, T., et al. 2020, ApJ, 892, 89
Lam, M. T., McLaughlin, M. A., Arzoumanian, Z., et al. 2019, ApJ, 872, 193
Lam, M. T., McLaughlin, M. A., Cordes, J. M., Chatterjee, S., &
  Lazio, T. J. W. 2018, ApJ, 861, 12
Lentati, L., Shannon, R. M., Coles, W. A., et al. 2016, MNRAS, 458, 2161
Levin, L., McLaughlin, M. A., Jones, G., et al. 2016, ApJ, 818, 166
Liu, K., Verbiest, J. P. W., Kramer, M., et al. 2011, MNRAS, 417, 2916
Madison, D. R., Cordes, J. M., Arzoumanian, Z., et al. 2019, ApJ, 872, 150
Manchester, R. N., Hobbs, G., Bailes, M., et al. 2013, PASA, 30, e017
Manchester, R. N., Hobbs, G. B., Teoh, A., & Hobbs, M. 2005, AJ, 129, 1993
McLaughlin, M. A. 2013, COGra, 30, 224008
Mingarelli, C. M. F., Lazio, T. J. W., Sesana, A., et al. 2017, NatAs, 1, 886
Ng, C. 2018, IAU Symp. 337, Pulsar Astrophysics the Next Fifty Years
   (Cambridge: Cambridge Univ. Press), 179
Ng, C., Pandhi, A., Naidu, A., et al. 2020, MNRAS, 496, 2836
Osłowski, S., van Straten, W., Bailes, M., et al. 2014, MNRAS, 441, 3148
Osłowski, S., van Straten, W., Demorest, P., et al. 2013, MNRAS, 430, 416
Perera, B. B. P., DeCesar, M. E., Demorest, P. B., et al. 2019, MNRAS,
  490, 4666
Phillips, J. A., & Wolszczan, A. 1991, ApJL, 382, L27
Ransom, S., Brazier, A., Chatterjee, S., et al. 2019, BAAS, 51, 195
```

```
Reardon, D. J., Hobbs, G., Coles, W., et al. 2016, MNRAS, 455, 1751
Rosado, P. A., Sesana, A., & Gair, J. 2015, MNRAS, 451, 2417
Sazhin, M. V. 1978, SvA, 22, 36
Shannon, R. M., & Cordes, J. M. 2010, ApJ, 725, 1607
Shannon, R. M., Osłowski, S., Dai, S., et al. 2014, MNRAS, 443, 1463
Siemens, X., Ellis, J., Jenet, F., & Romano, J. D. 2013, CQGra, 30, 224015
Sosa Fiscella, V., del Palacio, S., Combi, L., et al. 2021, ApJ, 908, 158
Taylor, J. H. 1992, RSPTA, 341, 117
Taylor, S., Ellis, J., & Gair, J. 2014, PhRvD, 90, 104028
Taylor, S. R., Vallisneri, M., Ellis, J. A., et al. 2016, ApJL, 819, L6
Testori, J. C., Reich, P., Bava, J. A., et al. 2001, A&A, 368, 1123
Thrane, E., & Romano, J. D. 2013, PhRvD, 88, 124032
Tiburzi, C., Verbiest, J. P. W., Shaifullah, G. M., et al. 2019, MNRAS,
  487, 394
van Straten, W. 2006, ApJ, 642, 1004
van Straten, W., Bailes, M., Britton, M., et al. 2001, Natur, 412, 158
Verbiest, J. P. W., Bailes, M., Coles, W. A., et al. 2009, MNRAS, 400,
Verbiest, J. P. W., Bailes, M., van Straten, W., et al. 2008, ApJ, 679, 675
Xin, C., Mingarelli, C. M. F., & Hazboun, J. S. 2020, arXiv:2009.11865
You, X. P., Hobbs, G. B., Coles, W. A., Manchester, R. N., & Han, J. L. 2007,
  ApJ, 671, 907
```